

Design and Performance Analysis of a Highly Efficient Polychromatic Full-Stokes Polarization Modulator for the CRISP Imaging Spectrometer

A.G. DE WIJN,¹ J. DE LA CRUZ RODRÍGUEZ,² G.B. SCHARMER,² G. SLIEPEN,² AND P. SÜTTERLIN²

¹High Altitude Observatory, National Center for Atmospheric Research, P.O. Box 3000, Boulder, CO 80307, USA

²Institute for Solar Physics, Department of Astronomy, Stockholm University, AlbaNova University Centre, SE-106 91, Stockholm, Sweden

ABSTRACT

We present the design and performance of a polychromatic polarization modulator for the CRisp Imaging SpectroPolarimeter (CRISP) Fabry-Perot tunable narrow-band imaging spectropolarimeter at the Swedish 1-m Solar Telescope (SST). We discuss the design process in depth, compare two possible modulator designs through a tolerance analysis, and investigate thermal sensitivity of the selected design. The trade-offs and procedures described in this paper are generally applicable in the development of broadband polarization modulators. The modulator was built and has been operational since 2015. Its measured performance is close to optimal between 500 and 900 nm, and differences between the design and as-built modulator are largely understood. We show some example data, and briefly review scientific work that used data from SST/CRISP and this modulator.

Keywords: instrumentation: polarimeters

1. INTRODUCTION

Our knowledge of solar magnetism relies heavily on our ability to detect and interpret the polarization signatures of magnetic fields in solar spectral lines. Consequently, new Stokes polarimeters are designed to have the capability to observe the solar atmosphere in a variety of spectral lines over a wide wavelength range. One immediate instrument requirement stemming from this need for wavelength diversity is that the polarization modulation scheme must be *efficient* at all wavelengths within the working range of the spectropolarimeter. (For the definition of polarimetric efficiency see [del Toro Iniesta & Collados 2000](#).) Typically, one attempts to achieve this goal by achromatizing the polarimetric response of a modulator. This, for instance, is the rationale behind the design of super-achromatic wave plates ([Serkowski 1974](#); [Samoylov et al. 2004](#); [Ma et al. 2008](#)). [Tomczyk et al. \(2010\)](#) argued that for many instruments achromaticity is too strong a constraint, and instead proposed the concept of the *polychromatic* modulator that is efficient at all wavelengths of interest, but has polarimetric properties that vary with wavelength.

In this paper, we present the development process of a modulator for the CRisp Imaging SpectroPolarimeter (CRISP) Fabry-Perot tunable narrow-band imaging instru-

ment ([Scharmer 2006](#); [Scharmer et al. 2008](#)) at the Swedish 1-m Solar Telescope (SST, [Scharmer et al. 2003](#)). First, we compare the performance of two possible modulator designs, and use a Monte-Carlo tolerance analysis to evaluate their robustness. We analyze the sensitivity of the modulator to thermal conditions, and present the opto-mechanical packaging and electrical interfaces. The modulator was constructed and tested at the High Altitude Observatory (HAO). We compare as-built properties to those of the design. Finally, we show some example polarimetric observations made using this modulator.

This modulator was designed and built to replace a modulator based on Liquid Crystal Variable Retarders (LCVRs). LCVRs are electro-optical devices that have a fixed fast axis orientation, but, as the name implies, can be set to any retardance within some range by applying an AC voltage. LCVRs generally have much slower switching speeds than Ferroelectric Liquid Crystals (FLCs). In contrast to LCVRs, FLCs have a constant retardance but switch their fast axis orientation between two states separated by a switching angle, typically around 45°. The LCVRs in the old CRISP modulator had to be “overdriven” and the modulator state order had to be optimized in order to switch during the 10 ms readout time of the CRISP cameras. More importantly, however, thermal sensitivities of the setup forced polarimetric calibration more frequently than desired ([van Noort & Rouppe van der Voort 2008](#)).

We limit ourselves to designs that use FLCs because their fast switching speed allows the state of the modulator to be

changed in less than the allotted 10 ms, thus allowing for the highest possible modulation rate. Fast modulation is desirable because seeing-induced crosstalk between Stokes parameters that is a dominant source of error in ground-based polarimeters is less at higher modulation rates (Lites 1987; Judge et al. 2004; Casini et al. 2012a). Also, it is of importance in maximizing the overall efficiency of the polarimeter. Many present-day CCD and CMOS detectors allow simultaneous exposure and readout so that the switching speed of the modulator becomes the limitation in the overall duty cycle—and thus efficiency—of the modulator.

For a recent review of instrumentation for solar spectropolarimetry we direct the reader to Iglesias & Feller (2019). Rodenhuis et al. (2014) present a more general review of instrumentation for measurements of polarized light.

2. DESIGN

A computer program was developed at HAO to determine component parameters for a given modulator design (Tomczyk et al. 2010). This program was used successfully to design the modulators for the ProMag, CoMP-S, SCD, Chromag, and UCOMP instruments built or under construction by HAO (Elmore et al. 2008; Kučera et al. 2010; Kucera et al. 2015; de Wijn et al. 2012). More recently, it, or similar programs derived from it or independently implemented by others, have been used to design modulators, e.g., for the DKIST (Harrington & Sueoka 2018). The code can use several different merit functions. We choose to minimize the maximum of the deviation of the modulation efficiency ϵ_Q , ϵ_U , and ϵ_V in Stokes Q , U , and V from the optimal value of $1/\sqrt{3}$ for balanced modulation at a number of user-specified wavelengths, normalized by the efficiency ϵ_I in Stokes I . It is possible to bias the modulation efficiency to prefer linear or circular polarization. However, such schemes are of limited use because the SST is not a polarization-free telescope (Selbing 2005).

We study two designs: one consisting of two FLC devices followed by one fixed retarder that we will refer to as the FFR design, and one consisting of an FLC, a fixed retarder, a second FLC, and a second fixed retarder that we will refer to as the FRFR design. The HAO-designed instruments mentioned above all use the FFR design. Others have implemented FRFR designs (e.g., Gandorfer 1999; Keller & Solis Team 2001; Iglesias et al. 2016) The FFR design has 5 free parameters, whereas the FRFR design has 7 (see Table 1). Both have significant freedom to optimize the design over wide wavelength ranges.

All modulators discussed here were optimized for balanced modulation, i.e., equal efficiency in Q , U , and V , at 16 equidistant wavelengths over the 500–900 nm operating wavelength range of the CRISP instrument. We allow the program to choose the retardances of the FLCs and the re-

Table 1. FRFR and FFR modulator designs. The orientation value of the FLCs refers to the bisector of the two fast axis positions that are separated by 45° .

Component	Retardance waves at 665 nm	Orientation degrees
FRFR		
FLC 1	0.429	0
Retarder 1	0.181	121.0
FLC 2	0.324	17.5
Retarder 2	0.543	109.6
FFR		
FLC 1	0.490	0
FLC 2	0.248	112.9
Retarder 1	0.228	108.8

tarders, as well as the orientations of the second FLC and the retarders. Experience has shown that the best configurations have an orientation very close to 0 or 90° with respect to the orientation of the analyzing polarizer for the bisector of the first FLC. We therefore fix the orientation of the first FLC at 0 degrees to eliminate one free parameter. The switching angle of an FLC is sensitive to both temperature and drive voltage (Gisler 2005; Gisler et al. 2003). Hence, we assume that we can adjust the drive voltage at a given operating temperature so that the FLC switching angles are 45 degrees. We also account for dispersion of birefringence for all elements of the modulator using measurements from similar optics.

The program can use several different optimization techniques. We first use a Latin Hypercube Sampling algorithm (McKay et al. 1979) to probe the parameter space. We use a large population size of 25,000 but only 5 iterations in which we shrink the parameter space around the best solution. We then apply a downhill simplex method (Nelder & Mead 1965) to refine the solution. To increase confidence that we did not find a local minimum, we repeat the search several times and check that we consistently find the same solution. The resulting designs are summarized in Table 1.

The next step is to evaluate the robustness of the design using a Monte-Carlo tolerancing method. Efficiencies were calculated for a total of 1000 modulator realizations with parameters chosen from a uniform distribution around the design values. The width of the distributions was chosen to be the vendor-supplied accuracies for the retardances of the devices of 50 nm for the FLCs and 2 nm for the retarder. For the orientation we assume an error of up to 1 degree. Experience has shown that alignment of the optics with this accuracy is possible by hand with a simple lab setup. The switching angle of the FLCs is assumed to be 45 degrees with insignificant error. FLCs typically have large manufacturing errors in their retardances. Since as-built retardances will be known prior to assembly of the modulator, the tolerancing

process re-optimizes the angles of the components after the retardances have been chosen.

As an example, a realization of the FFR modulator might have FLCs with retardances of 0.513 and 0.236 waves, and a retarder with a value of 0.243 waves, at the reference wavelength of 665 nm. The tolerancing procedure would then re-optimize the modulator design to find optimal angles of 115.5 and 109.9° for the second FLC and the retarder. Then, the procedure will perturb all the angles to account for mounting errors, to, say, -0.6 , 114.8, and 109.8°, and finally calculate the efficiencies of this modulator realization.

The resulting expected modulator performance is shown in Figs. 1 and 2. An even better result can be achieved by re-optimizing the retardances of the fixed retarders in addition to the orientations after the as-built FLC retardances are known. This was not pursued for the CRISP modulator due to time constraints, and because the design is shown to be tolerant to expected manufacturing errors.

Figures 1 and 2 show that both designs are well-behaved. The nominal FRFR design exhibits better overall performance than the FFR design, which is not surprising in view of its higher number of degrees of freedom. The tolerance analysis shows that the FRFR design is considerably less resistant to manufacturing errors than the FFR design, particularly in ϵ_V between 500 and 800 nm. We show this design here to demonstrate the importance of performing a tolerance analysis. It is possible to find other FRFR designs that have slightly worse performance, but are more robust against manufacturing errors. However, the FFR design performs very well over this wavelength range and has the benefit of one less component, and thus results in a thinner stack of optics with fewer interfaces. In our case, we select the FFR design primarily because the modulator must fit in a tight space in the existing CRISP optical setup.

There is considerable freedom to pick a reference wavelength. Our experience has shown that a wavelength at or slightly below the middle of the operational range is a good choice for practical reasons. Here, we picked 665 nm, also because the program chooses to use FLCs with retardances that are equal to $\lambda/2$ and $\lambda/4$ at that wavelength within the margin of error. We fix these components at those values out of convenience and optimize the fixed retarder and component orientations. We find that the orientation of the 2nd FLC does not change. The fixed retarder value and orientation change slightly to 0.225λ and 109.1 degrees.

FLCs with these specifications were procured from Citizen Finetech Miyota. The FLC used in these devices is MX8068. A polycarbonate retarder was procured from Meadowlark Optics.

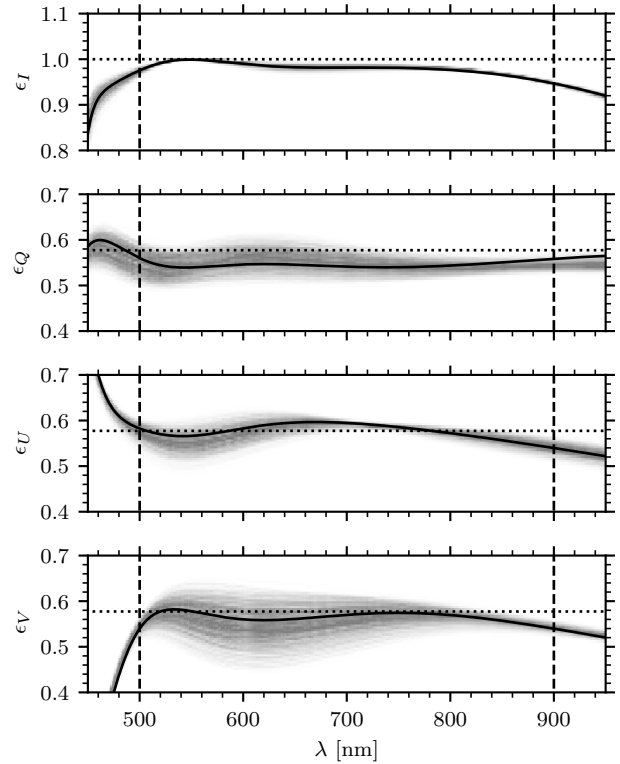


Figure 1. Theoretical I , Q , U , and V efficiencies with tolerances for the FRFR design. Solid curves: design performance of the modulator as a function of wavelength. Horizontal dotted lines: theoretical efficiencies for a perfectly balanced and optimally efficient modulator. Vertical dashed lines: lower and upper bound of the design wavelength range. The grayscale background shows the expected spread of performance as a result of component and construction tolerances.

The switching angle of FLCs is somewhat sensitive to temperature. [Gisler et al. \(2003\)](#) measured it as a function of temperature and found a mostly linear relationship with a coefficient of $-0.4^\circ/\text{K}$. This coefficient is specific to the FLC. [Gisler \(2005\)](#) shows an example measurement with a coefficient of $-0.41^\circ/\text{K}$. For this analysis we use the larger, more conservative value.

We evaluate the effect of temperature change of the modulator following a procedure similar to [Lites & Ichimoto \(2013\)](#). We follow the notation of [del Toro Iniesta & Colados \(2000\)](#) and refer the reader to that work for a rigorous mathematical treatment of polarimetric measurements. The Stokes vector \mathbf{S} is modulated into a vector of intensities \mathbf{I} . The modulation can be described by a modulation matrix \mathbf{O} ,

3. THERMAL ANALYSIS

$$\mathbf{I} = \mathbf{O}\mathbf{S}. \quad (1)$$

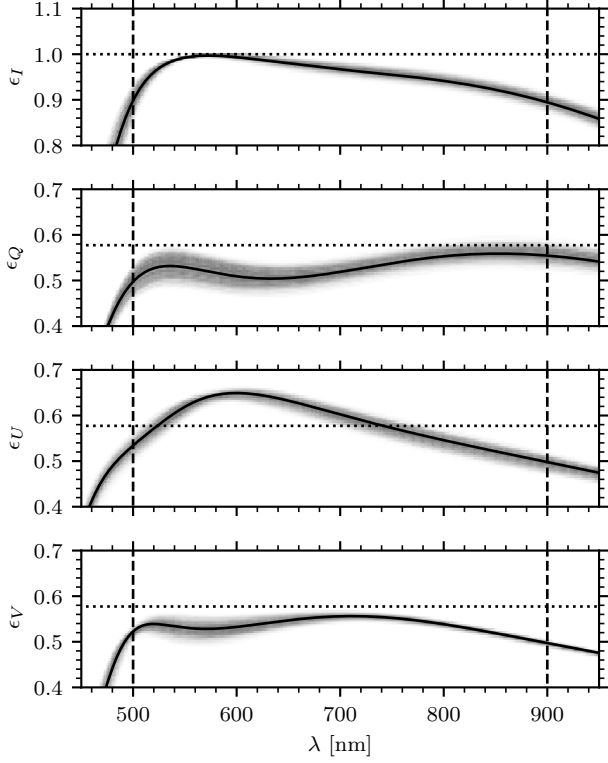


Figure 2. Theoretical I , Q , U , and V efficiencies with tolerances for the FFR design in the same format as Fig. 1

A demodulation matrix \mathbf{D} is used to recover the Stokes vector,

$$\mathbf{S} = \mathbf{D} \mathbf{I}. \quad (2)$$

A difference in temperature of the modulator during observations and calibrations will result in a mismatch of the modulation and demodulation matrices. We denote with \mathbf{O}' and \mathbf{D}' the modulation and demodulation matrices derived from the calibration, and with \mathbf{S}' the inferred Stokes vector,

$$\mathbf{S}' = \mathbf{D}' \mathbf{I}. \quad (3)$$

We can then relate the inferred Stokes vector \mathbf{S}' and the real Stokes vector \mathbf{S} through an error matrix,

$$\mathbf{S} = \mathbf{X} \mathbf{S}'. \quad (4)$$

It is easy to see that we now have

$$\mathbf{X} \mathbf{D}' = \mathbf{D}, \quad (5)$$

and using $\mathbf{D}' \mathbf{O}' = \mathbf{I}_4$ we find

$$\mathbf{X} = \mathbf{D} \mathbf{O}'. \quad (6)$$

For our error analysis, we can calculate the modulation matrix \mathbf{O}' from the unperturbed design, and demodulation matrices \mathbf{D} for several switching angles to determine the permissible change in temperature.

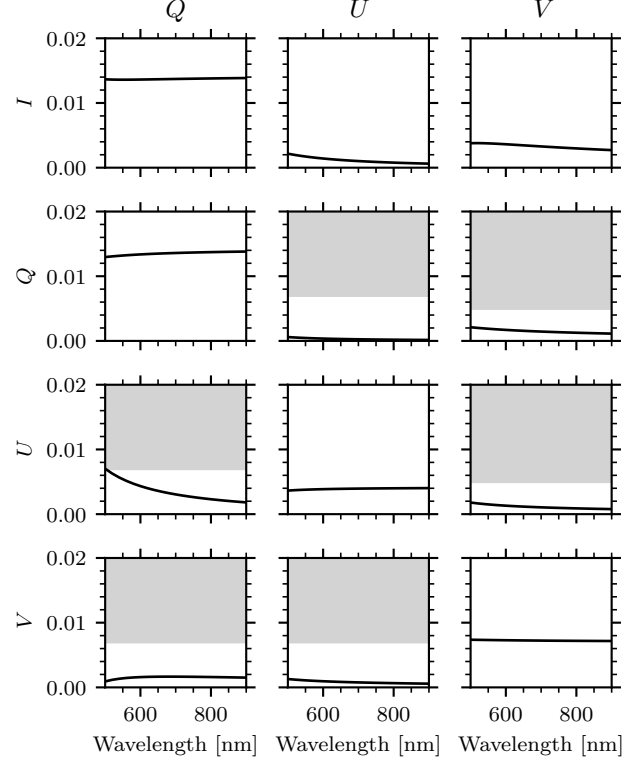


Figure 3. The $|\mathbf{X} - \mathbf{I}_4|$ matrix elements for the error introduced by 0.5 K change in temperature assuming a $-0.4^\circ/\text{K}$ coefficient for the switching angle of the FLCs. The first column of the matrix is omitted because it is identically 0. Gray areas are outside the limits given in Eq. 7.

Limits must be imposed on every element of the matrix \mathbf{X} . The diagonal elements represent a scale error that is much less sensitive than crosstalk errors. The scaling on I is unconstrained after normalizing \mathbf{S} by I . Furthermore, the elements in the Q and U columns can be scaled by the maximum expected linear polarization signal, and those in the V column can be scaled by the maximum expected circular polarization signal. We follow [Ichimoto et al. \(2008\)](#) and adopt maxima of $e = 0.001$ of I for the crosstalk error between Stokes Q , U , and V , $a = 0.05$ for scale error, $p_l = 15\%$ of I for linear polarization, and $p_v = 20\%$ of I for circular polarization. We then find

$$|\mathbf{X} - \mathbf{I}_4| \leq \begin{pmatrix} & 0.333 & 0.333 & 0.250 \\ 0.001 & 0.050 & 0.007 & 0.005 \\ 0.001 & 0.007 & 0.050 & 0.005 \\ 0.001 & 0.007 & 0.007 & 0.050 \end{pmatrix}, \quad (7)$$

where, e.g., the second and third element of the top row are given by the ratio a/p_l , and the second and third element of the last column are given by the ratio e/p_v .

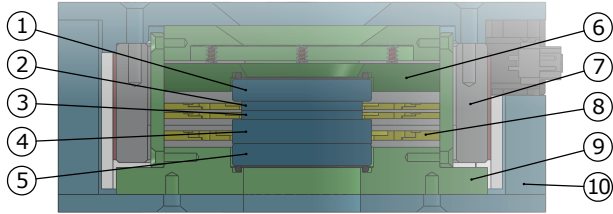


Figure 4. A cross-section view of the modulator with major components labeled. Optical components are shown in dark blue: 1. entrance window; 2. FLC 1; 3. FLC 2; 4. fixed retarder; and 5. exit window. The mechanical assembly is color-coded by its major components: 6. pressure plate (dark green); 7. oven (gray); 8. optic holders (yellow); 9. inner mount assembly (light green); and 10. Delrin shell (light blue). See the text for details on the mechanical design.

Figure 3 shows the $\mathbf{X} - \mathbf{I}_4$ matrix elements for the error introduced by the change in switching angle for a 0.5 K change in temperature. The Q -to- U term is the worst offender and is just below the limit at 500 nm.

There are other contributors to \mathbf{X} than changes in switching angle with temperature. E.g., the retardances of the FLCs and the retarder also have a small temperature dependence. The polarimetric calibration procedure also has a finite accuracy (van Noort & Rouppe van der Voort 2008). We do not explicitly model these effects here, since the switching angle is expected to be the dominant source of error. For example, polycarbonate retarders have typical temperature coefficients around 0.4 pm/nm/K, and a 5 K change in temperature is required to exceed the permissible error. Instead we assign a fraction of the permissible error to changes in switching angle and set the requirement for thermal stability to ± 0.2 K.

4. OPTO-MECHANICAL DESIGN

Figure 4 shows a cross-section of the modulator. The mechanical design borrows heavily from the HAO Lyot filter designs used in the CoMP, CoMP-S, SCD, and ChroMag instruments. The modulator optics are glued into mounts that allow the optic to be oriented to any angle using a RTV silicone. The mounts consist of two parts. The inner part is round and holds the optic. It can be oriented to the desired angle and glued to the hexagonal outer part that is indexed to the inner mount assembly. The optics stack is assembled between parallel windows using index-matching gel. The windows rest on O-rings in their mounts. The entrance window mount is spring-loaded against the inner mount assembly with 4.4 N.

The inner mount assembly is inserted in an oven consisting of an aluminum tube with a silicone rubber heater element and aerogel insulation wrapped around it. An off-the-shelf precision temperature controller is used to stabilize the oven to 35.0°C to better than 0.1°C. The modulator is encased in a

Delrin housing. Electrical connections for the FLCs and the heater system are routed to two D-subminiature connectors on the housing.

A custom controller based on an Arduino Uno micro-controller board was built to drive the FLCs. The camera software sends a voltage sequence to the controller via a serial interface, which is preloaded into two Burr-Brown DAC714 digital-to-analog converters (DACs). A synchronization pulse is then used to update the voltages when the chopper that controls the exposure of the cameras is closed. The FLCs are primarily capacitive loads, with capacitance of about 80 nF. The DACs are capable of driving 5 mA, which is more than adequate to drive the FLCs between states in under a millisecond. The controller also resets the voltage to zero after a few seconds of inactivity as a safety feature because the FLCs may be damaged if driven by a constant voltage for a prolonged period of time.

5. PERFORMANCE

The components of the modulator must be accurately aligned to ensure proper functioning of the assembled device. HAO has a facility Lab Spectropolarimeter (LSPM) test setup for polarimetric characterization of optics that was used to test components of the CRISP modulator after they were mounted.

The LSPM consists of relay optics that feed light from a halogen bulb through, in order, a calibration package that consists of a polarizer and a retarder in individual rotation stages, the sample under test, and a polychromatic polarization modulator and analyzer, into an Ocean Optics USB4000 fiber-fed spectrograph. This setup allows for characterization of the full Mueller matrix of the sample as a function of wavelength. The spectrograph covers the wavelength range from about 450 nm to about 1100 nm, though signal levels are low under 550 nm.

We solve for retardance and fast axis position of a linear retarder that matches the Mueller matrices derived from LSPM measurements as a function of wavelength. Figure 5 shows the results for the three CRISP modulator components. The figure also shows the design retardances and fast axis positions. The $\lambda/2$ and $\lambda/4$ FLCs have measured retardances of 0.47λ and 0.24λ at 665 nm, and mean switching angles of 48.2° and 46.7° . The fixed retarder is measured at 0.251λ . All three components show a curious increase in the fast axis position at the shortest wavelengths. However, the signal level is low, and it may be that the effect is the result of systematic errors in the measurement.

As discussed in Sect. 2, we can re-optimize the design with these values. However, we made our measurements at room temperature. The measurement should have been performed at the operating temperature of 35°C because component retardance has some temperature dependence. Using the re-

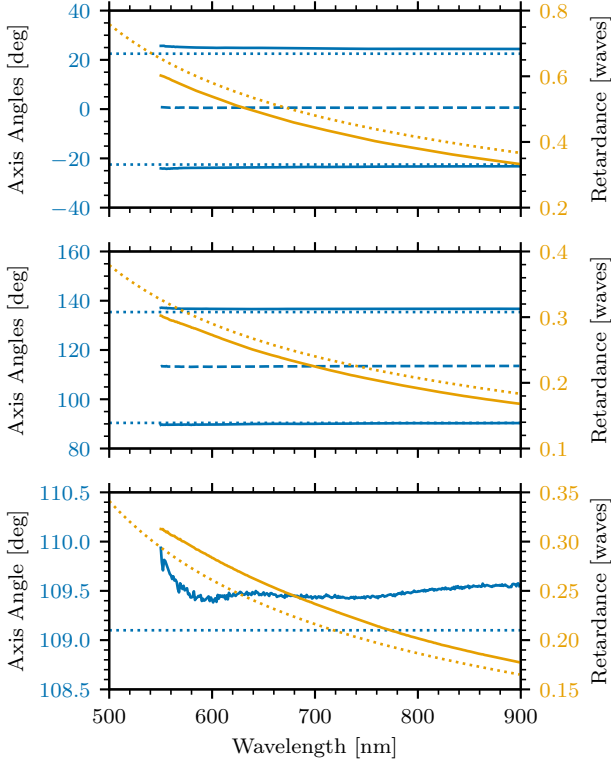


Figure 5. Solid lines: retardances (orange) and fast axis positions (blue) of the $\frac{1}{2}$ -wave FLC (top panel), the $\frac{1}{4}$ -wave FLC (middle panel), and the retarder (bottom panel), as determined by a fit to the Mueller matrix inferred from LSPM measurements at room temperature. The panels for the FLCs show two fast axis positions for ± 8 V drive voltages. Dashed lines: fast axis bisector. Dotted lines: design retardances and fast axis positions. In these measurements the signal level drops below acceptable levels around 550 nm.

tardance values at room temperature we find fast axis angles for the 2nd FLC and the fixed retarder are 113.5 and 108.5 degrees. However, if we assume the retarder will have its design retardance at 35°C, the fast axis positions revert to the nominal design. The FLC switching angles are larger than the nominal 45° design, but also expected to decrease at a higher operating temperature, possibly to angles below 45° (Gisler et al. 2003; Gisler 2005). We choose not to change the modulator design because of the unknown effect of temperature on the component retardance and FLC switching angle, and because only marginal improvement of performance is expected.

The modulator was first assembled with air gaps, and once the proper relative alignment of the components was confirmed using the LSPM, the modulator was assembled in its housing using Nye OCF-452 optical coupling fluid on the glass interfaces. The purpose of the coupling fluid is to reduce internal Fresnel reflections between the surfaces of the

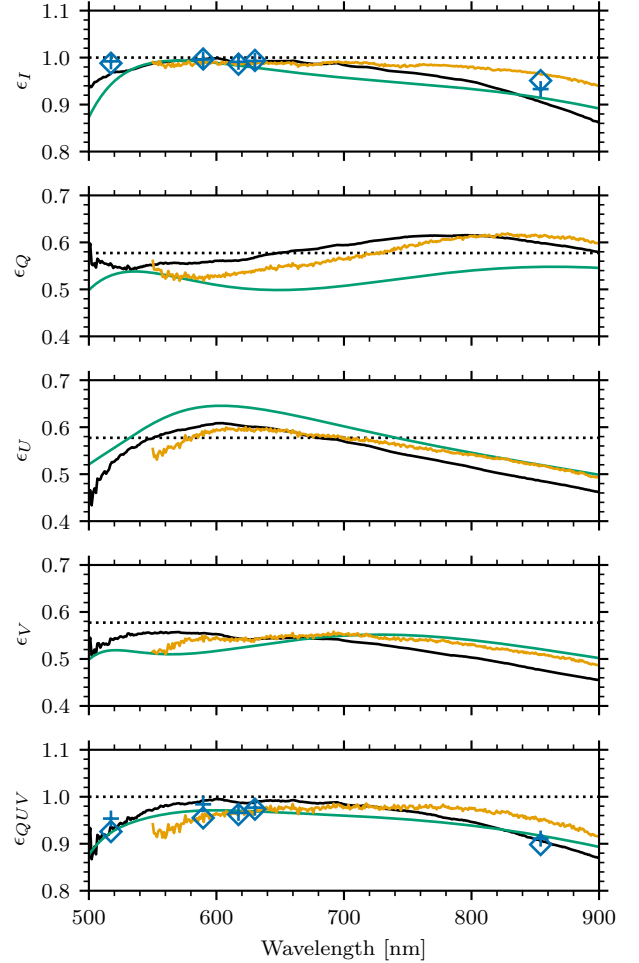


Figure 6. Modulation efficiencies of the modulator. The top four panels shows the efficiency in Stokes I , Q , U , and V . The bottom panel shows the RSS of the efficiencies in Stokes Q , U , and V . Solid black lines: modulation efficiencies of the assembled modulator measured with the LSPM. Solid green lines: design efficiencies. Solid orange lines: modulation efficiencies expected from the measurements in Fig. 5. Blue crosses and diamonds: modulation efficiencies measured at the telescope in the transmitted and reflected beams, resp. The horizontal dotted line in each panel shows the theoretical maximum efficiency for a balanced modulation scheme.

optics. Nye OCF-452 was used because it has a refractive index that is well-matched to the Corning XG glass of the FLCs and the BK7 glass of the retarder and windows. Internal Fresnel reflections at the optical interfaces of the components are limited to below the 2×10^{-5} level.

The fully assembled modulator was brought to operating temperature and tested again on the LSPM. The LSPM produces measurements of the Mueller matrix of the modulator in each of its 4 states. We simulate a perfect analyzer in Q to calculate modulation efficiencies, shown as a function of wavelength in Fig. 6.

The measured efficiencies largely show the expected behavior when compared to the design shown in solid green curves in Fig. 6. However, differences in the model and measured efficiencies cannot be fully attributed to as-built retardances and component alignment. The differences are likely due to several factors that were not included in the tolerance analysis. The model assumes that the components are perfect retarders with a known dispersion of birefringence, and that the FLCs have an exact 45° switching angle. In reality, the components have imperfections such as chromatic variation of the fast axis, and the actual dispersion of birefringence is different from the model. This can be seen in Fig. 5. The solid blue lines are not horizontal, and the solid and dotted orange lines are not parallel. The FLC switching angle is also not exactly 45° . Lastly, bulk rotational alignment of the modulator to the analyzer was not included in the analysis. The efficiencies of some modulator designs, in particular the traditional rotating retarder, are invariant under rotation of the modulator with respect to the analyzer. This design is not invariant, and rotation of the modulator results in depressed efficiencies.

Figure 6 also shows the modulation efficiencies computed from the Mueller matrices of the measured components in orange. They show good agreement with the measured efficiencies of the assembled modulator. We attribute the differences mostly to the components not being measured at operating temperature. There are also likely small differences in the relative orientation of the components in the assembled modulator compared to the individual measurements.

The CRISP instrument is intended for high-resolution imaging. The modulator, therefore, must have low transmitted wavefront distortion (TWD). Because the internal optics are coupled using an index-matching gel, the TWD is dominated by the entrance and exit windows. Fortunately, excellent quality windows are inexpensive and commonly available. The TWD of the assembled modulator was measured using a Zygo interferometer. It was found to be 0.20 waves at 632 nm RMS over the clear aperture after removal of the tilt component, but including 0.14 waves of power that introduces primarily a shift in focus position.

The modulator was installed at the SST in October 2014. CRISP uses a polarizing beamsplitter to analyze the polarization signal in two orthogonal directions simultaneously (de la Cruz Rodríguez et al. 2015). This kind of setup is known as a dual-beam polarimeter and allows for the removal of crosstalk resulting from atmospheric seeing from Stokes I to Stokes Q , U , and V (Casini et al. 2012a). Measured modulation efficiency averaged over the field of view for the transmitted and reflected beams at five wavelengths commonly used for solar polarimetry are given in Table 2 and also shown in Fig. 6 as blue crosses and diamonds.

Table 2. Modulation efficiencies measured at the telescope averaged over the field of view.

Wavelength	ϵ_I	ϵ_Q	ϵ_U	ϵ_V	ϵ_{QUV}
Transmitted					
517.3 nm	0.992	0.500	0.588	0.560	0.954
589.6 nm	0.996	0.573	0.591	0.539	0.984
617.3 nm	0.991	0.506	0.608	0.554	0.966
630.2 nm	0.993	0.576	0.579	0.536	0.977
854.2 nm	0.933	0.570	0.504	0.501	0.911
Reflected					
517.3 nm	0.988	0.485	0.572	0.543	0.926
589.6 nm	0.997	0.557	0.572	0.524	0.955
617.3 nm	0.986	0.506	0.607	0.549	0.962
630.2 nm	0.994	0.576	0.579	0.530	0.974
854.2 nm	0.951	0.563	0.497	0.493	0.898

It is not possible to directly compare the efficiencies in the individual Stokes parameters. The telescope measurements include all the optics on the tables, which include a number of mirrors and lenses, a dichroic beamsplitter, the CRISP pre-filter, a gray beamsplitter, and the CRISP etalons. These elements cannot be separated from the modulator. The calibration procedure fits all optics on the table between the calibration optics and the polarization analyzer as one modulation matrix (van Noort & Roupe van der Voort 2008). In effect, all optical elements between the calibration optics and the polarimetric analyzer together act as the modulator. There are oblique reflections that may cause some mixing of all Stokes parameters due to retardance of the mirror coatings, and the reference frame of polarization of these measurements is not normal to the optical table. It is still valuable to compare the performance in the telescope to the design performance and lab measurements, but this can only be done in an aggregate way, i.e., by comparing the RSS of the efficiencies in Stokes Q , U , and V ,

$$\epsilon_{QUV} = \sqrt{\epsilon_Q^2 + \epsilon_U^2 + \epsilon_V^2}. \quad (8)$$

The overall agreement of the performance in the telescope setup and the assembled modulator is very good. The largest difference in the RSS of the efficiencies in Q , U , and V is 3.7% in the reflected beam at 589.6 nm.

The transmitted and reflected beams show very similar behavior. The differences in efficiencies between the beams are on the order of a few percent, and may result from differences in the contrast of the polarizing beamsplitter in the transmitted and reflected beams, or from polarizing components in the telescope such as the wide-band beamsplitter that has a highly uneven ratio of the transmitted and reflected light.

The overall performance is excellent with the lowest efficiencies only slightly below 50% (cf. the optimum and bal-

anced efficiency of 57.7%). The RSS of the efficiencies in Stokes Q , U , and V are 94%, 97%, 96%, 98%, and 90% for these 5 wavelengths.

6. CONCLUSION

The trade-offs and procedures described in this paper were employed to design the polarimetric modulator for the CRISP instrument, but can be applied to the design of modulators for other instruments. We chose to omit some steps that could result in somewhat improved performance of the modulator. If schedule permits, it is possible to incrementally optimize the design with measured optic properties. We could have delayed the purchase of the retarder until the FLCs, which have the largest errors, had been characterized at operating temperature, so that the value of the retarder could have been optimized for the as-built FLCs. While this design with only three components is robust, such incremental re-optimization may be necessary to guarantee acceptable efficiencies for modulator designs with more optical elements that cover larger wavelength ranges (Snik et al. 2012).

We did not specifically consider polarized spectral “fringes” in our design process. A description of polarized spectral fringes can be found in reviews by Lites (1991), Semel (2003), and Clarke (2004). They are interference patterns that are produced by reflections between parallel surfaces in a system with polarization optics, such as the components of the modulator, that are difficult to characterize (Harrington et al. 2017) and remove (Rojo & Harrington 2006; Casini et al. 2012b; Casini & Li 2019). Snik et al. (2015) optimized components to suppress polarized fringes for their application by ensuring that the periods of the fringes are much smaller than the spectral resolution of their instrument. This approach cannot be applied in modulators using FLCs (or LCVRs) because the FLC layer thickness that determines the period of the fringes is set by the required retardance. Because the FLC layer is very thin, fringes caused by reflections at the FLC-glass interfaces have periods of ten or more of nanometers (Gisler et al. 2003), i.e., much larger than the CRISP bandpass of less than ten picometers (Scharmer et al. 2008). These fringes will consequently be relatively stable over the CRISP bandpass and therefore will be nearly completely removed in the polarimetric calibration. Fringes caused by reflections between surfaces at larger optical distance have smaller periods and can be a problem. For those, the only available option is to reduce the amplitude of fringes by reducing the amplitude of Fresnel reflections from the interfaces of the optical elements. The use of optical coupling fluid is therefore not only required to address etaloning, but also to suppress these fringes.

The polarimetric modulator described here has been in use for science observations at the SST starting with the 2015 observing season. Example data of a sunspot are shown in

Fig. 7. The data reduction procedures are described in detail by de la Cruz Rodríguez et al. (2015) and Löfdahl et al. (2018). These data can be fit using forward-modeling procedures to derive quantitative measures of atmospheric parameters, most notably the strength and direction of magnetic field. For example, Kuridze et al. (2018) studied the structure and evolution of temperature and magnetic field in a flaring active region using full-Stokes CRISP observations in the Ca II line at 854.2 nm, Vissers et al. (2019) used similar data in combination with data from the IRIS mission (De Pontieu et al. 2014) to study Ellerman bombs and UV bursts, Vissers et al. (2020) inferred the photospheric and chromospheric magnetic field vector in a flare target and studied their differences, Libbrecht et al. (2019) used CRISP observations in the He I D₃ line in a study of a flare, Morosin et al. (2020) and Pietrow et al. (2020) studied chromospheric magnetic fields in plage targets and estimated a canopy mean field strength of 400 G in the chromosphere, and Joshi et al. (2020) studied very small-scale reconnection in the solar photosphere using CRISP polarimetry and CHROMIS (Scharmer et al. 2019) observations in H β .

Figure 8 shows a region of quiet sun with the line-of-sight component of the magnetic field inferred from full-Stokes observations of the Fe I 617.3 nm line profile using a spatially-regularized Milne-Eddington inversion method (de la Cruz Rodríguez 2019). This example highlights the power of CRISP combined with this modulator. Quiet-sun magnetic fields are weak and difficult to detect. Telescopes and instruments that achieve high spatial resolution, have adequate spectral resolving power, and have high system efficiency are required to study them. We refer the interested reader to Bellet Rubio & Orozco Suárez (2019) for a comprehensive review of observations of quiet-sun magnetic field.

The high throughput and efficiency of CRISP with this modulator also enables observations in many lines with polarimetry while maintaining sufficient cadence for studies of dynamic events. Such multi-line observations were used by Leenaarts et al. (2018) in a study of chromospheric heating in an emerging flux region. They used the STiC code (de la Cruz Rodríguez et al. 2019) to simultaneously interpret the signals from several lines. Esteban Pozuelo et al. (2019) used the same code in a similar way to study penumbral microjets.

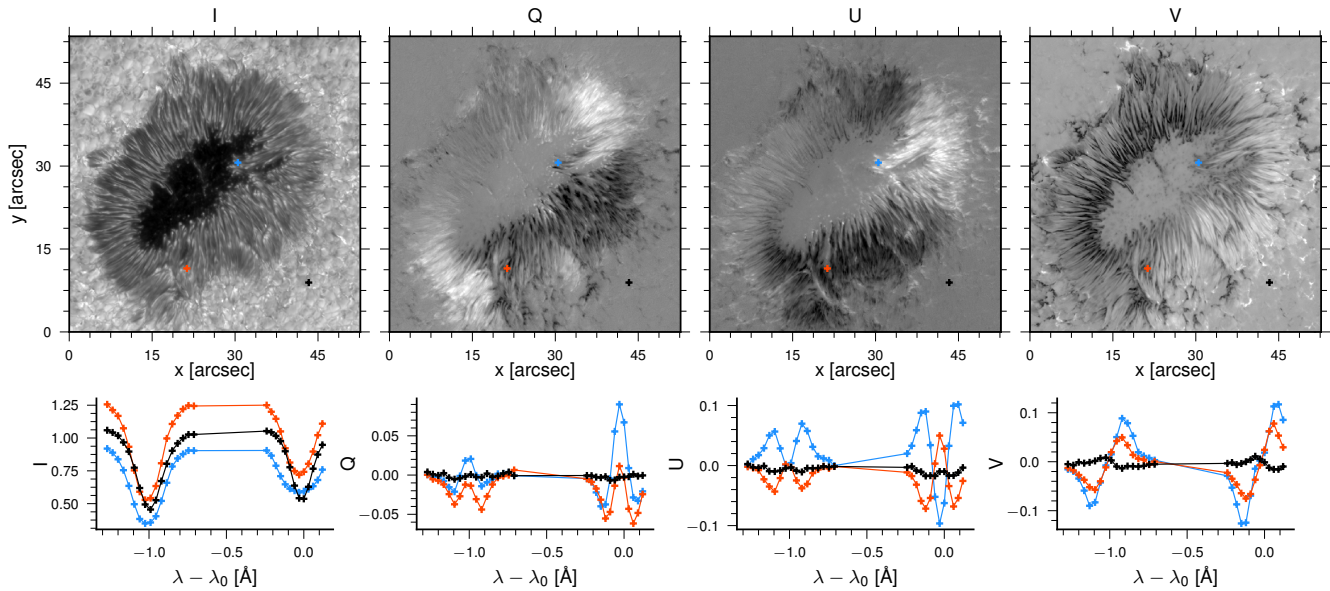


Figure 7. Example spectro-polarimetric data of AR12471 in the Fe I lines at 630.2 nm. The observation was recorded on 2019-05-10 around 09:10 UT. Top row: images of the Stokes parameter in the blue wing of the 630.25 nm line at -90 mÅ from line center. Spectra at the black, red, and blue crosses are shown in the bottom row. The locations of the spectral sampling are indicated by crosses.

ACKNOWLEDGMENTS

We acknowledge R. Casini for the development of the codes used for optimization and tolerancing of the modulator designs. This material is based upon work supported by the National Center for Atmospheric Research, which is a major facility sponsored by the National Science Foundation under Cooperative Agreement No. 1852977. CRISP and the modulator were funded by the Marianne and Marcus Wallenberg Foundation. This research has made use of NASA's Astrophysics Data System, NumPy (van der Walt et al. 2011), matplotlib, a Python library for publication quality graphics (Hunter 2007), Astropy, a community-developed core Python package for Astronomy (Astropy Collaboration et al. 2018, 2013), and the IPython package (Perez & Granger 2007). The acknowledgements were compiled using the Astronomy Acknowledgement Generator.

REFERENCES

- Astropy Collaboration, Price-Whelan, A. M., Sipőcz, B. M., et al. 2018, *AJ*, 156, 123
- Astropy Collaboration, Robitaille, T. P., Tollerud, E. J., et al. 2013, *A&A*, 558, A33
- Bellot Rubio, L. & Orozco Suárez, D. 2019, *Living Reviews in Solar Physics*, 16, 1
- Casini, R., de Wijn, A. G., & Judge, P. G. 2012a, *ApJ*, 757, 45
- Casini, R., Judge, P. G., & Schad, T. A. 2012b, *ApJ*, 756, 194
- Casini, R. & Li, W. 2019, *ApJ*, 872, 173
- Clarke, D. 2004, *Journal of Optics A: Pure and Applied Optics*, 6, 1036
- de la Cruz Rodríguez, J. 2019, *A&A*, 631, A153
- de la Cruz Rodríguez, J., Leenaarts, J., Danilovic, S., & Uitenbroek, H. 2019, *A&A*, 623, A74
- de la Cruz Rodríguez, J., Löfdahl, M. G., Sütterlin, P., Hillberg, T., & Rouppe van der Voort, L. 2015, *A&A*, 573, A40
- De Pontieu, B., Title, A. M., Lemen, J. R., et al. 2014, *SoPh*, 289, 2733

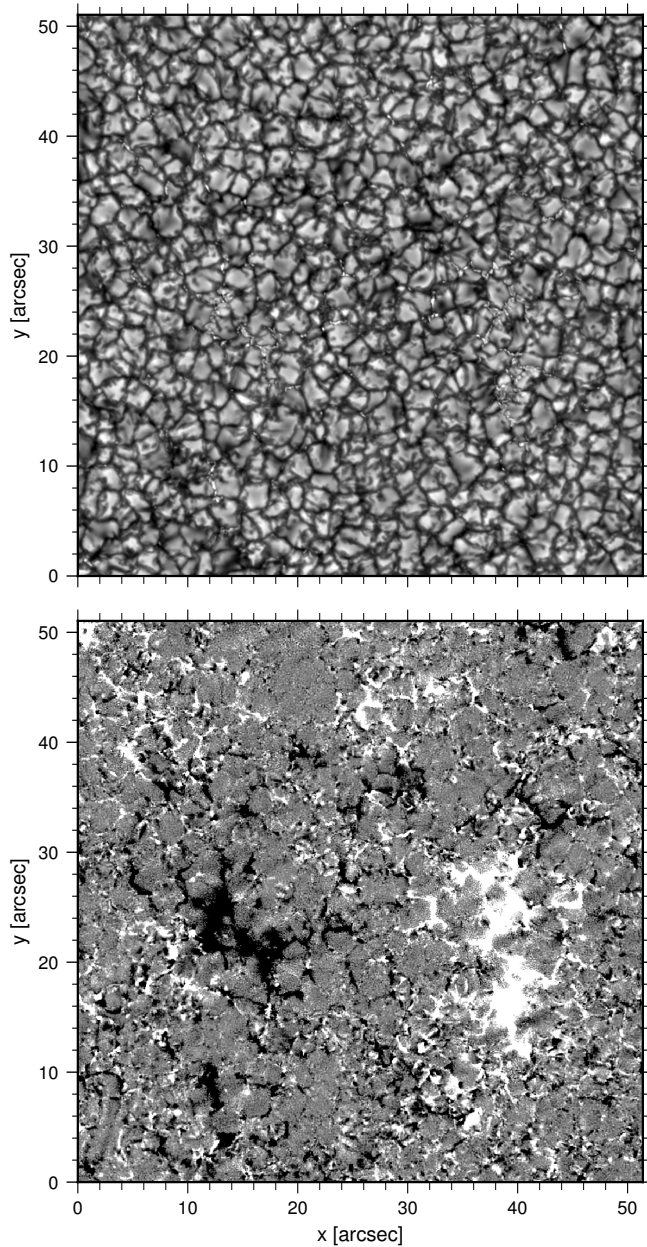


Figure 8. Intensity and line-of-sight magnetic field strength for a quiet sun region observed on 2020-07-14 around 08:41 UT during a period of very good seeing conditions. The magnetic field strength was inferred from observations of the Fe I 617.3 nm line and is scaled between -25 and 25 G.

de Wijn, A. G., Bethge, C., Tomczyk, S., & McIntosh, S. 2012, in Society of Photo-Optical Instrumentation Engineers (SPIE) Conference Series, Vol. 8446, Ground-based and Airborne Instrumentation for Astronomy IV, 844678

del Toro Iniesta, J. C. & Collados, M. 2000, *ApOpt*, 39, 1637

- Elmore, D. F., Casini, R., Card, G. L., et al. 2008, in Society of Photo-Optical Instrumentation Engineers (SPIE) Conference Series, Vol. 7014, Ground-based and Airborne Instrumentation for Astronomy II, 701416
- Esteban Pozuelo, S., de la Cruz Rodríguez, J., Drews, A., et al. 2019, *ApJ*, 870, 88
- Gandorfer, A. M. 1999, *Optical Engineering*, 38, 1402
- Gisler, D. 2005, PhD thesis, ETH Zurich
- Gisler, D., Feller, A., & Gandorfer, A. M. 2003, in Society of Photo-Optical Instrumentation Engineers (SPIE) Conference Series, Vol. 4843, Proc. SPIE, ed. S. Fineschi, 45–54
- Harrington, D. M., Snik, F., Keller, C. U., Sueoka, S. R., & van Harten, G. 2017, *Journal of Astronomical Telescopes, Instruments, and Systems*, 3, 048001
- Harrington, D. M. & Sueoka, S. R. 2018, *Journal of Astronomical Telescopes, Instruments, and Systems*, 4, 044006
- Hunter, J. D. 2007, *Computing in Science and Engineering*, 9, 90
- Ichimoto, K., Lites, B., Elmore, D., et al. 2008, *SoPh*, 249, 233
- Iglesias, F. A. & Feller, A. 2019, *Optical Engineering*, 58, 082417
- Iglesias, F. A., Feller, A., Nagaraju, K., & Solanki, S. K. 2016, *A&A*, 590, A89
- Joshi, J., Rouppe van der Voort, L. H. M., & de la Cruz Rodríguez, J. 2020, *A&A*, 641, L5
- Judge, P. G., Elmore, D. F., Lites, B. W., Keller, C. U., & Rimmele, T. 2004, *ApOpt*, 43, 3817
- Keller, C. U. & Solis Team. 2001, in *Astronomical Society of the Pacific Conference Series*, Vol. 236, Advanced Solar Polarimetry – Theory, Observation, and Instrumentation, ed. M. Sigwarth, 16
- Kucera, A., Tomczyk, S., Rybak, J., et al. 2015, in *IAU General Assembly*, Vol. 29, 2246687
- Kuridze, D., Henriques, V. M. J., Mathioudakis, M., et al. 2018, *ApJ*, 860, 10
- Kučera, A., Ambróz, J., Gömöry, P., Kozak, M., & Rybák, J. 2010, *Contributions of the Astronomical Observatory Skalnaté Pleso*, 40
- Leenaarts, J., de la Cruz Rodríguez, J., Danilovic, S., Scharmer, G., & Carlsson, M. 2018, *A&A*, 612, A28
- Libbrecht, T., de la Cruz Rodríguez, J., Danilovic, S., Leenaarts, J., & Pazira, H. 2019, *A&A*, 621, A35
- Lites, B. W. 1987, *ApOpt*, 26, 3838
- Lites, B. W. 1991, in *Solar Polarimetry*, ed. L. J. November, 166–172
- Lites, B. W. & Ichimoto, K. 2013, *SoPh*, 283, 601
- Löfdahl, M. G., Hillberg, T., de la Cruz Rodríguez, J., et al. 2018, *arXiv e-prints*, arXiv:1804.03030
- Ma, J., Wang, J.-S., Denker, C., & Wang, H.-M. 2008, *ChJA&A*, 8, 349
- McKay, M. D., Beckman, R. J., & Conover, W. J. 1979, *Technometrics*, 21, 239

- Morosin, R., de la Cruz Rodríguez, J., Vissers, G. J. M., & Yadav, R. 2020, arXiv e-prints, arXiv:2006.14487
- Nelder, J. A. & Mead, R. 1965, *The Computer Journal*, 7, 308
- Perez, F. & Granger, B. E. 2007, *Computing in Science and Engineering*, 9, 21
- Pietrow, A. G. M., Kiselman, D., de la Cruz Rodríguez, J., et al. 2020, arXiv e-prints, arXiv:2006.14486
- Rodenhuis, M., Snik, F., van Harten, G., Hoeijmakers, J., & Keller, C. U. 2014, in *Society of Photo-Optical Instrumentation Engineers (SPIE) Conference Series*, Vol. 9099, *Polarization: Measurement, Analysis, and Remote Sensing XI*, ed. D. B. Chenault & D. H. Goldstein, 90990L
- Rojo, P. M. & Harrington, J. 2006, *ApJ*, 649, 553
- Samoylov, A. V., Samoylov, V. S., Vidmachenko, A. P., & Perekhod, A. V. 2004, *JQSRT*, 88, 319
- Scharmer, G. B. 2006, *A&A*, 447, 1111
- Scharmer, G. B., Bjelksjo, K., Korhonen, T. K., Lindberg, B., & Petterson, B. 2003, in *Innovative Telescopes and Instrumentation for Solar Astrophysics*, ed. S. L. Keil & S. V. Avakyan, Vol. 4853, *International Society for Optics and Photonics (SPIE)*, 341 – 350
- Scharmer, G. B., Löfdahl, M. G., Sliepen, G., & de la Cruz Rodríguez, J. 2019, *A&A*, 626, A55
- Scharmer, G. B., Narayan, G., Hillberg, T., et al. 2008, *ApJL*, 689, L69
- Selbing, J. 2005, Master's thesis, Stockholm Univ., arXiv:1010.4142
- Semel, M. 2003, *A&A*, 401, 1
- Serkowski, K. 1974, *Methods of Experimental Physics*, 12, 361
- Snik, F., van Harten, G., Alenin, A. S., Vaughn, I. J., & Tyo, J. S. 2015, in *Society of Photo-Optical Instrumentation Engineers (SPIE) Conference Series*, Vol. 9613, *Polarization Science and Remote Sensing VII*, 96130G
- Snik, F., van Harten, G., Navarro, R., et al. 2012, in *Society of Photo-Optical Instrumentation Engineers (SPIE) Conference Series*, Vol. 8446, *Ground-based and Airborne Instrumentation for Astronomy IV*, 844625
- Tomczyk, S., Casini, R., de Wijn, A. G., & Nelson, P. G. 2010, *ApOpt*, 49, 3580
- van der Walt, S., Colbert, S. C., & Varoquaux, G. 2011, *Computing in Science and Engineering*, 13, 22
- van Noort, M. J. & Rouppe van der Voort, L. H. M. 2008, *A&A*, 489, 429
- Vissers, G. J. M., Danilovic, S., de la Cruz Rodríguez, J., et al. 2020, arXiv e-prints, arXiv:2009.01537
- Vissers, G. J. M., de la Cruz Rodríguez, J., Libbrecht, T., et al. 2019, *A&A*, 627, A101